$Mn_3Ag_{(1-x)}Cu_{(x)}N$ antiperovskite thin films with ultra-low temperature coefficient of resistance.

Cecil Cherian Lukose, Guillaume Zoppi and Martin Birkett*,

*Corresponding Author – martin.birkett@northumbria.ac.uk

Faculty of Engineering and Environment, Northumbria University,
Newcastle upon Tyne, NE1 8ST, UK.

Highlights

- First report on the reactive sputter deposition and post-deposition heat treatment of $Mn_3Ag_{(1-x)}Cu_{(x)}N$ thin films for ultra-low TCR application.
- Increasing Cu doping concentration in $Mn_3Ag_{(1-x)}Cu_{(x)}N$ controls stabilization of the manganese oxide upper surface layer.
- The extent of upper surface oxidation and crystallization of the underlying thin film are competing events to fine tune the electrical properties.
- Optimising the post-deposition heat treatment temperature results in TCR values better than ±5ppm/˚C and resistance stability of less than 1%.

Abstract

We demonstrate the first successful attempt to partially substitute Cu into the Mn_3AgN-antiperovskite system to form $Mn_3Ag_{(1-x)}Cu_{(x)}N$ thin films with ultra-low temperature coefficient of resistance (TCR) for fabrication of ultra-precise passive components. Films were grown by reactive magnetron sputtering on alumina and glass substrates and were found to be amorphous in nature with highly negative TCR of -233 to -351ppm/˚C in their as-grown state. Increasing Cu alloying from x=0 to 1, resulted in increased sheet resistance, a negative shift of TCR and a change of grain morphology from spherical to elongated. Post-deposition heat treatment at 300-375˚C, resulted in a positive shift of TCR and an ultra-low TCR of -4.66ppm/˚C for films with x=0.6. The heat treatment induces grain growth, surface roughness and the formation of a manganese oxide upper surface layer up until temperatures of 350˚C, after which surface oxidation begins to dominate. The growth rate of the surface layer is controlled by the Cu concentration and heat treatment temperature, which both play a central role in the development of these novel ultra-low TCR $Mn_3Ag_{(1-x)}Cu_{(x)}N$ thin film structures.

Graphical abstract

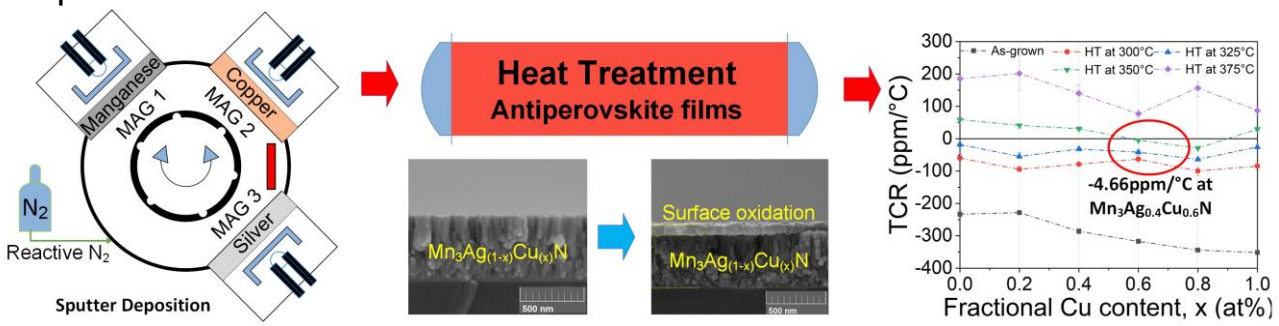

Keywords

Antiperovskite; thin film; sputter deposition; annealing; surface oxidation; near-zero TCR.

1. Introduction

Since their introduction in 1930 by Moral [1], antiperovskite structures have come a long way in their development. In particular, the antiperovskite structure with the general formula Mn_3AN (where A is a transition metal) has gained renewed interest because of its unique properties such as magnetoresistance [2-4], giant magnetocaloric effects [3, 4], zero and negative thermal expansion [3, 5-8], magnetostriction [9, 10], superconductivity [4, 11], supercapacitance [12], spin glass behaviour [13], and extremely low temperature coefficient of resistance (TCR) [14-16]. These properties make Mn_3AN a potential material system for application in electrical actuators and sensors[17], solid state electrolytes in batteries [18-20], high precision measurement [11, 12, 21] and hybrid electronic devices [22]. Mn_3AN has a very stable octahedron unit, where six manganese (Mn) atoms bond with the nitrogen (N) atom in the centre of the cell, but the metal atoms at the corner of the unit are loosely bound as seen in figure 1 [23-25]. The stable octahedron is the result of strong hybridization between 2p orbitals of N and 3d orbitals of Mn and creates a narrow band near the fermi level [3, 14]. The occupation of these narrow bands is very sensitive to the number of valance electrons, contributed by the transition metal species that are introduced at the cubic corners. This fact allows for introduction of various metallic atoms at the cubic corners, thereby causing significant change in the electronic and magnetic transport properties of the material [26].

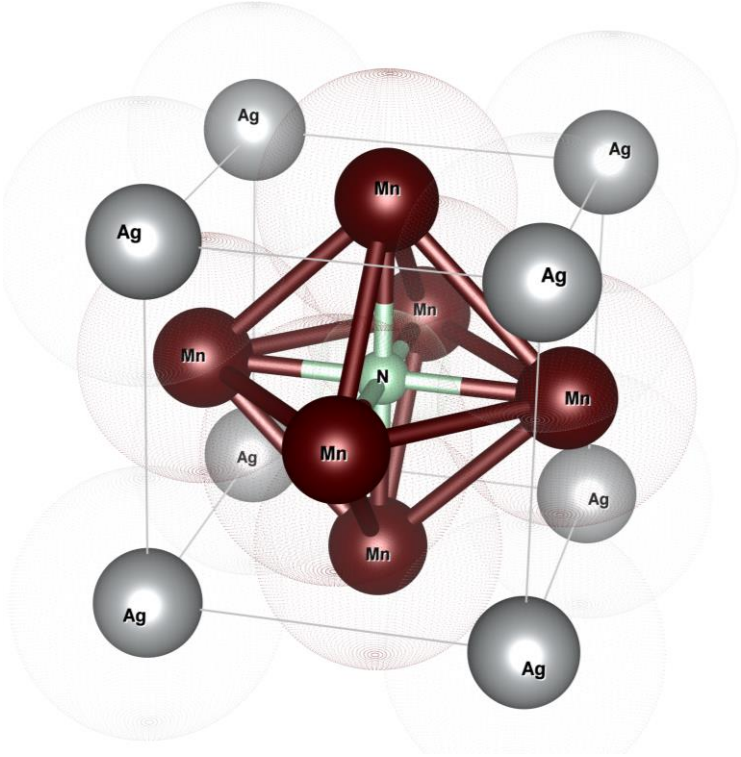

Figure 1 Unit cell projection of stoichiometric Mn_3AgN antiperovskite structure showing local coordination environment of Mn atoms forming stable octahedron (drawn with VESTA visualisation software).

Chi *et al.* suggested that Mn-based antiperovskite structures, in particular Mn_3CuN can be utilised in fabrication of high precision electrical components because of its high electrical resistivity of 20 µΩ-m, very low TCR of 46 ppm/˚C and good stability in air [22]. Materials with very low TCR values are very useful for fabrication of high precision components within electronic systems like global positioning systems (GPS) [27], data storage solutions [28], thermo-electrical devices [28, 29] and in temperature and flow control sensors for automobile applications [30]. Some of the early efforts were made by Ding *et al.* and Takenaka *et al.* to tune the electrical properties and further reduce TCR values in bulk structures of Mn_3NiN and Mn_3AgN by alloying with copper [27, 31, 32]. For the $Mn_3Ni_{0.7}Cu_{0.3}N$ composition, stable and reproducible TCR values of 22 ppm/˚C were achieved [27], and TCR values as low as 6 ppm/˚C were reported for $Mn_3Ag_{0.68}Cu_{0.32}N$ [31], making these materials more promising for low TCR applications than commercially available materials like Manganin or Constantan [33]. This was further improved to an ultra-low TCR value of 0.42 ppm/˚C and a resistance drift rate of only 9.1 µΩ/Ω/year [32].

Although some excellent results have been achieved to date for Mn-based antiperovskite structures in bulk form [27, 31, 32], sample fabrication has only been achieved by solid state sintering techniques, in which a weighed amount of Mn is fired along with other doping elements in a sealed nitrogen environment at very high temperature of the order of 700-800 ˚C [3]. Although this method can yield high quality crystals, it is renowned for being difficult to control as the use of high temperature leads to dissociation of nitrogen [34] while not being suitable for manufacturing rate production [3, 14]. On the other hand, some attempts have been made to study Mn-based antiperovskite structures like Mn_3CuN and Mn_3NiN [10, 26, 34] in thin film form but none include partial substitution by a third element like Ag or Cu, to achieve ultra-low TCR values on ceramic substrates like alumina as used commonly in the fabrication of real world passive components. In this work, we demonstrate for the first time, the sputter deposition and heat treatment of Mn_3AgCuN antiperovskite thin film structures with TCR values better than 5 ppm/˚C and sheet

resistance and stability values comparable to the well-established Ni-Cr material systems [35], thereby, opening potential application within ultra-precise thin film passive component fabrication.

2. Materials and methods

$Mn_3Ag_{(1-x)}Cu_{(x)}N$ films with values of x varying from 0 to 1 in steps of 0.2, were sputter deposited using a Teer Coatings UDP 350 sequential deposition system. The thin films were deposited on standard soda lime glass slides (75 x 25 x 1 mm^3) which were pre-cleaned in diluted Decon 90 solution for 2 minutes and then rinsed with double deionised water followed by nitrogen blow dry. Prescribed alumina substrates (101.6 x 101.6 x 1 mm^3, see figure 2) having 135 individual specimen circuits (10.16 x 6.35 mm^2) in 15 rows x 9 columns, were also loaded into the deposition chamber along with the glass slides. Silver conductor pads were screen printed, dried and fired onto each individual circuit to aid electrical contact. Part of the conductor pads were then screen printed with a water-soluble mask to provide a site for soldering wire connections after thin film deposition. Thin films deposited on glass slides were used to perform structural, chemical and morphological characterization, whereas thin films deposited on alumina substrates were used for electrical studies.

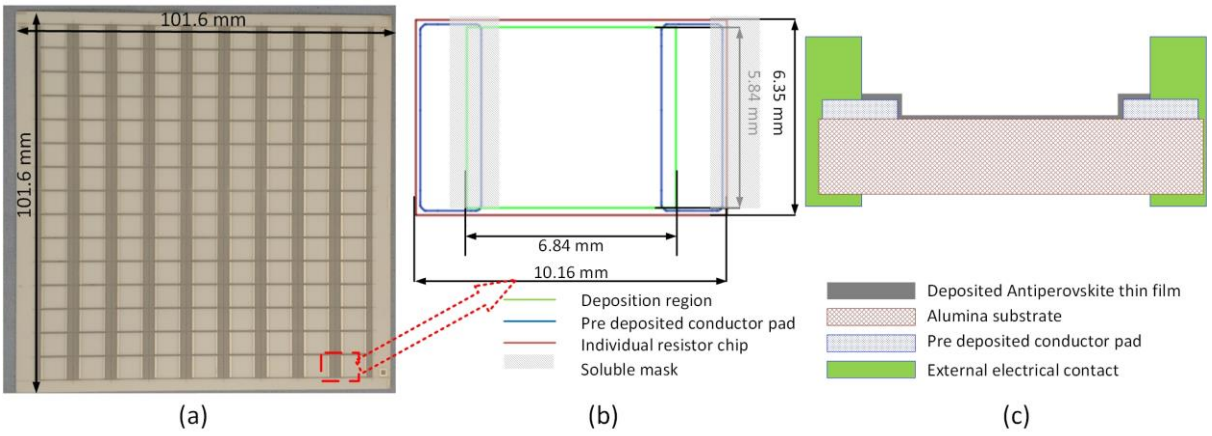

Figure 2 a) Prescribed alumina substrate with 135 individual circuits; 2b) dimensions of individual resistor circuit with soluble silicone mask partially covering the conductor pads; 2c) cross sectional view of individual resistor circuits after thin film deposition.

Sputtering was performed from three individual targets of Mn (99.95%), Ag (99.99%) and Cu (99.99%) with the substrates rotating sequentially over each target on a central carousel. A constant RF power of 300 W was applied on the circular Mn target (100 mm diameter), while the DC power levels applied on the circular Ag (100 mm diameter) and rectangular Cu (248 x 133 mm^2) targets were varied from 0 to 37 W and 0 to 28 W, respectively to achieve the required atomic compositions. All depositions were carried out at a constant working pressure of 0.3 Pa, by introducing high purity N_2:Ar mixture. The partial pressure of N_2 in the N_2:Ar mixture was varied from 10.0 to 16.6 % with increasing Cu doping concentration to maintain the required stoichiometry in the deposited thin films. Target to substrate distance was 130 mm and a constant rotation speed of 5 rpm was maintained for a total deposition duration of 90 minutes. No substrate heating was provided during deposition.

Following removal from the deposition chamber, the thin film samples were subjected to heat treatment in a tube furnace from 300 to 375 ˚C for 3 hours under a N_2 flow (2 L/min) to fine tune their TCR property. A second stage of heat treatment was then performed on the samples in an open-air environment at 260 ˚C for 16 hours to improve their electrical resistance stability.

Electrical, structural and morphological studies were performed on as-grown and heat-treated thin film samples to understand the effect of Cu incorporation and heat treatment condition. Electrical resistance was measured by the 4-wire Kelvin method using an Agilent 3458 digital multimeter electrically connected to the thin film via a pair of wires soldered to pre-deposited conductor pads on either end of the alumina substrate, see figure 2c. The TCR values were measured by immersing the samples into mineral oil at 20 and 70˚C in a Grant LTC1 oil bath with a GD120 thermostat and measuring the resistance value at each temperature setting. Electrical properties were measured for 5 thin film circuits selected from the four corners and centre of the alumina substrate and the values averaged. Dry heat stability tests were performed on samples after the stabilization stage of heat treatment. For this test, samples were left at 155 ˚C in an open-air oven for 168 hours (1 week) and resistance changes were measured every 24 hours.

Crystallinity and structural characterization of the thin film samples was determined by X-ray diffraction (XRD) using a Siemens D5000 diffractometer (Cu Kα radiation, λ=1.54 Å) for a 2θ range of 20˚ to 90˚ in steps of 0.02˚. Film thickness was measured with a Bruker Dektak XT stylus profilometer, by rastering the tip over six different sites of the step pattern created by Kapton tape on the glass substrates and the values averaged thereafter. Surface roughness and film morphology were studied using a Veeco Dimension 3100 Atomic force microscopy (AFM) system in contact mode over a 3 x 3 μm^2 area. The film cross sections and surface morphology were studied using a Tescan MIRA 3 scanning electron microscope (SEM). Elemental compositions were determined by averaging the values from 5 sites across the glass samples, using an Oxford Instruments X-Max 150 energy dispersive X-ray (EDX) detector within the SEM operated at 15 KeV (5 KeV for low voltage measurements). Depth profiling was performed using secondary ion mass spectroscopy (SIMS) from a Hidden Analytical gas ion gun (Argon) rastered over a 500 x 500 μm^2 area and a quadruple detector.

3. Results and discussion

3.1 Electrical characterization

The as-grown thickness of the Mn_3AgN (i.e. x = 0) films was measured as 560 ±12 nm and decreased with increasing Cu content to a minimum thickness of 498 ±10 nm for the Mn_3CuN (i.e. x = 1) films, as shown in Table 1. This reduction in thickness can be related to the higher deposition rate and larger radii of Ag when compared to Cu [36]. The results from quantitative EDX analysis of the films are also presented in Table 1. Films from either extremes (x = 0 and 1), were slightly deficient in Mn but the required stoichiometric ratio of 3:1:1 $Mn:Ag_{(1-x)}Cu_{(x)}:N$ was achieved for all target compositions to within ±3 at.%.

Table 1: Thickness and chemical composition of the as-grown $Mn_3Ag_{(1-x)}Cu_{(x)}N$ films with increasing Cu concentration from 0 to 1 and reducing Ag concentration from 1 to 0 at.%

Target values		As-grown values achieved		
Composition	**X experimental**	**Mn:Ag:Cu:N (at.%)**	**Composition**	**Thickness (nm)**
Mn_3AgN	0	57:20:0:23	$Mn_{2.85}AgN_{1.15}$	560 ±12
$Mn_3Ag_{0.8}Cu_{0.2}N$	0.2	59:15:5:21	$Mn_{2.95}Ag_{0.75}Cu_{0.25}N_{1.05}$	545 ±18
$Mn_3Ag_{0.6}Cu_{0.4}N$	0.4	61:14:6:19	$Mn_{3.05}Ag_{0.7}Cu_{0.3}N_{0.95}$	523 ±13
$Mn_3Ag_{0.4}Cu_{0.6}N$	0.6	60:9:11:20	$Mn_3Ag_{0.45}Cu_{0.55}N_1$	529 ±23
$Mn_3Ag_{0.2}Cu_{0.8}N$	0.8	60:4:17:19	$Mn_3Ag_{0.2}Cu_{0.85}N_{0.95}$	532 ±16
Mn_3CuN	1.0	57:0:23:20	$Mn_{2.8}Cu_{1.2}N$	498 ±10

Figure 3(a) shows the average values of sheet resistance and TCR measured for the six sets of $Mn_3Ag_{(1-x)}Cu_{(x)}N$ thin films with increasing Cu concentration. The average value of sheet resistance increases from 7.0±1.5 Ω/□ to 21.9±1 Ω/□ as the concentration of Cu in the film increases from x=0 to 1. This gradual increase can be explained as a combinatorial effect of the 12% reduction in film thickness from Ag rich to Cu rich films and the higher bulk resistivity of Cu (1.7×10^{-8} Ωm at 300K) compared to Ag (1.6×10^{-8} Ωm at 300K) [37]. The transition metals in their bulk forms have a positive TCR in the order of 1000s of ppm/˚C, however, TCR values of thin film structures are known to be very different from their bulk counterparts because of surface scattering and grain boundary effects becoming dominant and making the TCR negative [38]. As shown in figure 3(a), the TCR value is seen to become progressively negative with increasing Cu concentration from -233±10 ppm/˚C for Mn_3AgN to -351±6 ppm/˚C for Mn_3CuN. This reduction in resistivity with increasing temperature indicates that $Mn_3Ag_{(1-x)}Cu_{(x)}N$ follows the semiconductor type of electrical conductivity [26]. Substitution of Ag by Cu at the corner sites of the antiperovskite unit cell, results in a reduction in valance electron contribution towards the narrow band near the fermi level, which in turn leads to a reduction in carrier density, observed as an increasingly negative value of TCR [24]. Results of the dry heat resistance stability test for all six film compositions is also shown in figure 3(a) with drastic improvements with increasing Cu concentration down to 0.85% for x = 1. The stability value of 0.85% is very promising [35] and this value can be improved by adding further layers of protection resin coatings similar to process stages from a thin film resistor (TFR) fabrication cycle to improve the resistance stability value of high precision resistors [39].

Figure 3(b) shows the changes in sheet resistance of each thin film composition after heat treatment at 300 to 375 ˚C in steps of 25 ˚C. A sustained increasing trend can be seen for the sheet resistance of all six compositions with increasing heat treatment temperature. Within each composition, these films at first show a slight decrease in the value of sheet resistance for heat treatment temperature up to 325 ˚C and with further increment in temperature, an increase in the sheet resistance is observed. Previous work by Jui-chang *et al.* showed a proportional reduction in film resistivity with increasing annealing temperature caused by grain growth and healing of defects and sputter deposition damage, whereas work done by De Los Santos Valladares *et al.* showed a competing

effect which increases the sheet resistance due to oxidation of the film at higher temperatures [40-43]. Therefore, it is reasonable to expect that for treatment temperatures below 325 ˚C, defect healing and crystallization of films lead to a reduction in R_s but thereafter the surface oxidation overcomes these effects and results in an increase in R_s. TCR values for the thin films with increasing heat treatment temperature from 300 to 375 ˚C for 3 hours in N_2 are shown in figure 3(c). With each increment in the heat treatment temperature, the TCR values move closer to the zero TCR line. The TCR remains negative for all thin film compositions for heat treatment up to 325 ˚C. The zero TCR crossover point lies between 325 and 350 ˚C for films with x = 0.0, 0.2 and 0.4 and between 350 and 375 ˚C for films with x=0.6, 0.8 and 1.0 (figure 3c inset). The most favourable value of TCR is observed to be -4.66 ppm/˚C for $Mn_3Ag_{0.45}Cu_{0.55}N$ (i.e. x = 0.6) films after heat-treatment at 350 ˚C. The lowest average TCR value achieved for Mn_3AgN and Mn_3CuN films are -18 and -25 ppm/˚C, respectively, after heat-treatment at 325 ˚C.

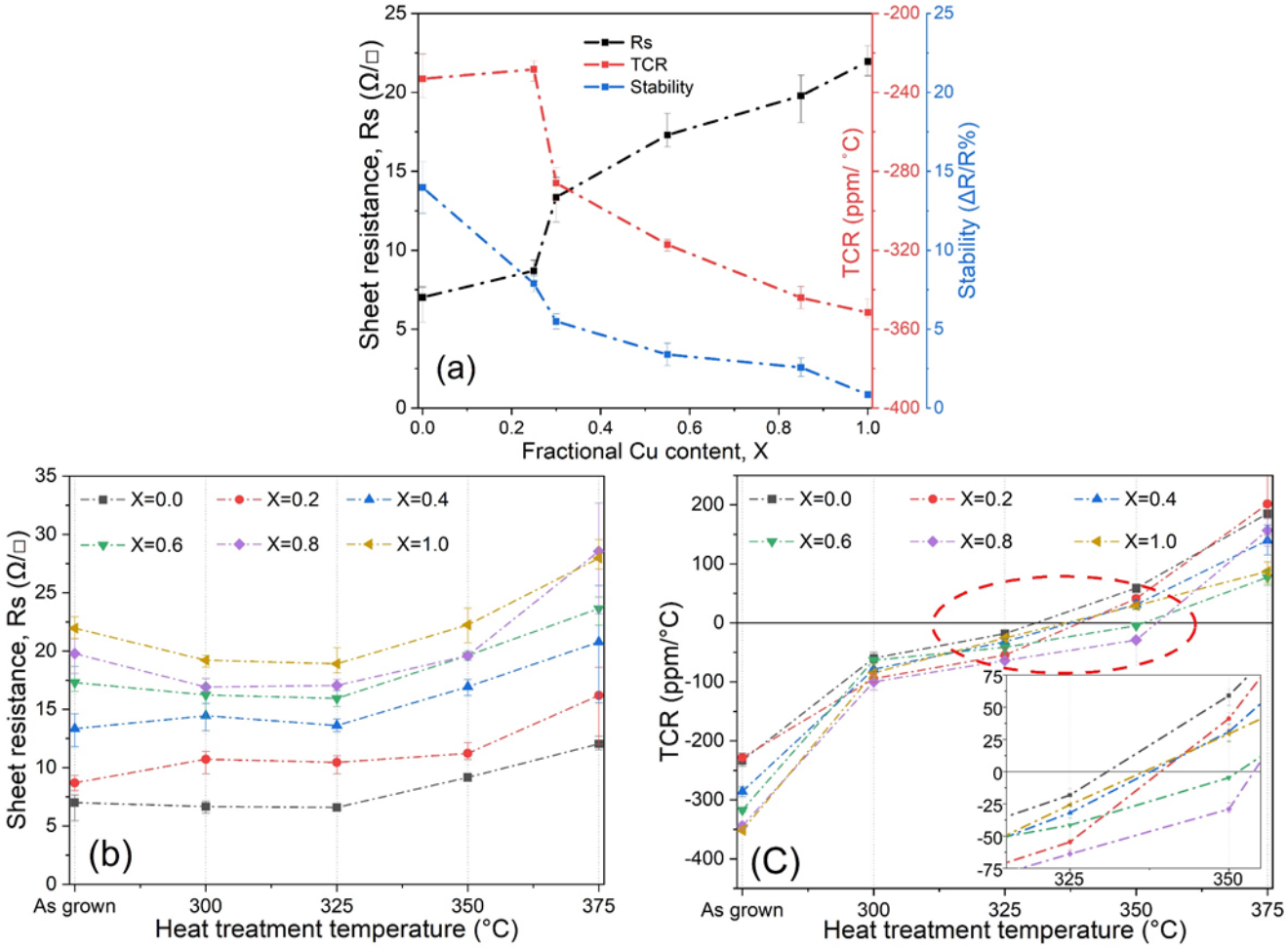

Figure 3: (a) As-grown electrical properties of films with increased Cu in $Mn_3Ag_{(1-x)}Cu_{(x)}N$. (b) Sheet resistance and (c) TCR of $Mn_3Ag_{(1-x)}Cu_{(x)}N$ films as-grown and after heat treatment. Inset: zero TCR crossover temperature for films with increasing Cu doping.

3.2 Structural characterization

To understand the mechanisms responsible for the changes in electrical properties, structural characterization was performed using XRD for the as-grown $Mn_3Ag_{(1-x)}Cu_{(x)}N$ thin films, see figure 4(a). For films with x = 0, only a small protrusion close to 38.8° is visible, which is the expected (111)

peak location for the Mn_3AgN structure (ICSD CC 52592). For films with x=0.2, peaks belonging to (111) and (200) planes are visible, though they are observed to be broad covering the Mn_3AgN and Mn_3CuN (ICSD CC 628356) peak positions. With further increments in Cu concentration, (x=0.4 and 0.6), a peak at θ=46.64˚, identifiable as the (200) plane of the Mn_3CuN antiperovskite structure becomes dominant and a further shift in peak position towards higher angles is observed. This shift is the result of the substitution of Ag by Cu, which has a comparatively smaller radii and induces a reduction in lattice parameter [44, 45]. For Cu rich films (x=0.8 and 1), no crystalline peaks were observed which is not surprising as the development of the (200) peak of Mn_3CuN requires a substrate temperature above 75˚C, as seen in the earlier works by Y.Na et al [10], and the thin films in this work were grown at room temperature (~25˚C) with no substrate heating. For all as-grown films, no other manganese, silver, copper or their nitride phases are observed, confirming that the as-grown films exist in the pure antiperovskite phase.

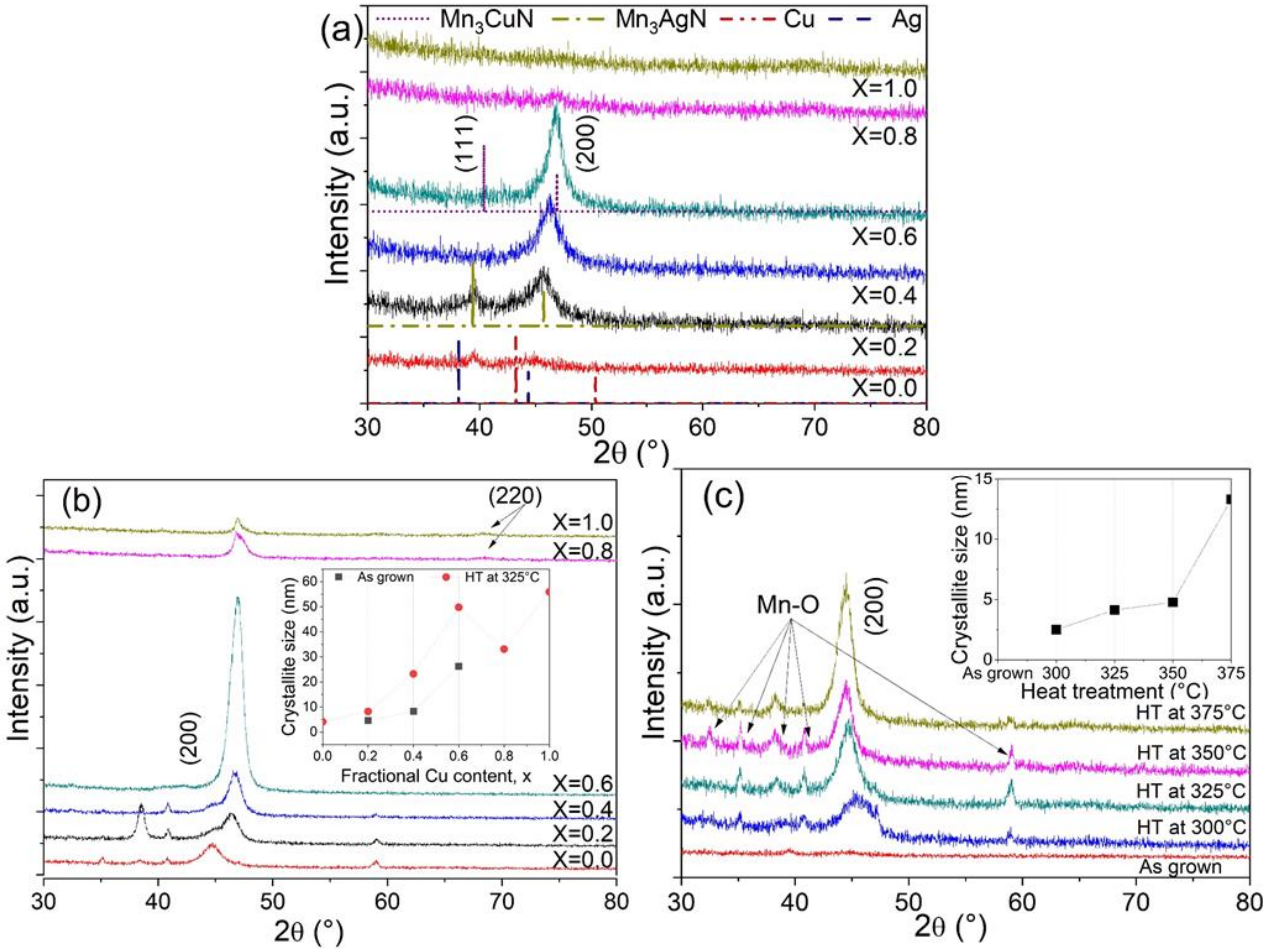

Figure 4: (a) XRD spectrum for as-grown $Mn_3Ag_{(1-x)}Cu_{(x)}N$ films with increasing concentration of Cu. (b) XRD spectra of $Mn_3Ag_{(1-x)}Cu_{(x)}N$ after heat treatment at 325˚C; inset: change in (200) crystallite size as a function of x for as-grown and heat-treated at 325˚C films. (c) XRD spectra comparing Mn_3AgN films in as-grown and heat-treated states; Inset: (200) crystallite size change for Mn_3AgN films with increasing heat treatment temperature.

Figures 4(b) shows the XRD spectrum following heat treatment at 325˚C. It can be clearly seen that films from all six compositions show crystallization, even the films with x = 0.8 and 1 which didn't show any clear peaks in their as-grown state. With increasing Cu concentration there is a gradual migration from the (200) plane of Mn_3AgN structure at 45.1˚ to the (200) plane for Mn_3CuN at 46.6˚. For films with x = 0, after heat treatment at this temperature, peaks representing (200) planes at 45.1˚ become sharper and more pronounced than the peak at 38.8˚ for as-grown films. From figure

4b, it is clear that films with x = 0.6 are the most crystalline, which is also the composition that achieved the best TCR value of -4.66ppm/˚C. The absence of any other peaks suggests that the structure remains stable in the antiperovskite phase, as Cu starts replacing Ag in the lattice. The films with x = 1.0, exist in a pure Mn_3CuN antiperovskite phase with preferential arrangement along the (200) plane. Heat-treated Cu rich samples (x = 0.8 and 1.0) begin to show a weak additional peak at 68.1˚, which is representative of the (220) plane of the Mn_3CuN antiperovskite structure.

Variation of crystallite size with increasing Cu concentration in the films for (200) peak, calculated using Scherrer's equation [46], is shown in the inset of figure 4(b). For the as-grown samples, films with x=0.0, 0.8 and 1.0 did not register a clear peak to permit crystallite size calculations, while for films with x=0.2 and 0.4, the crystallite sizes were calculated to be 4.6 and 8.3 nm, respectively. Films with x=0.6, show the largest crystallite size at 26.2 nm growing to 49.8 nm after heat treatment. Other compositions follow a similar trend and register a growth in crystallite size following heat treatment (inset of figure 4(b). These XRD spectra and crystallite size calculations support the theory that heat treatment leads to crystallization of the film structure, which is manifested as lower sheet resistance at heat treatment temperatures up to 325˚C. Figure 4(c) shows that for the same composition (x=0), with increase in heat treatment temperature, the diffraction peaks become sharper suggesting that crystallization further improves. Crystallite size calculations (inset of figure 4(c)) for these spectra were found to be 2.51, 4.14, 4.78, and 13.3 nm for heat treatment temperatures of 300, 325, 350 and 375˚C respectively. This trend of increasing crystallite size with heat treatment temperature leads to increases in the scattering effect or decreases the carrier mobility across the grain boundaries and is manifested as the positive shift in the temperature dependence of resistivity line shown in figure 3(b) [10, 14].

The formation of manganese oxide in the upper layers of the films is suggested as the main driver for the increase in sheet resistance at temperatures from 325°C upwards. Four peaks of lower intensities at 32.4, 35.2, 40.8 and 58.9˚ are becoming visible in figure 4(b). However, by comparing these to the XRD spectra of x=0 films heat-treated from 300 to 375°C in figure 4(c), it can be seen these peaks become sharper for temperatures above 325˚C and are identified to be manganese oxide, MnO_x [47]. This observation, together with crystallite size calculations, further supports the hypothesis that for heat treatment temperatures up to 325°C the rate of oxidation is slow, and crystallization of the films is the main driver for the reduction in sheet resistance, but for temperatures from 350°C, higher rates of oxidation lead to increases in the sheet resistance. A higher number of MnO_x peaks are seen for the x = 0 films, and the number of MnO_x peaks diminish as the concentration of Cu increases in the film from x = 0 to 1. Ag has a tendency to precipitate out of thin film structures at high temperatures [48-51] and this combined with the higher reactivity of Mn compared to Ag, leads to preferential formation of MnO in the upper surface layer of the films [52]. Only the Manganese oxide peak at 32.4˚ is observed in the XRD spectra of Cu rich films, when heat-treated at temperatures higher than 350˚C. These claims are further supported by the cross-sectional imaging and surface chemical analysis of the films (see next section).

3.3 Morphological characterization

Three compositions were selected for further morphological analysis using SEM, two from either end of the composition spectrum x = 0 (Mn_3AgN) and x = 1 (Mn_3CuN) and x = 0.6 ($Mn_3Ag_{0.4}Cu_{0.6}N$) for its lowest observed TCR value of -4.66 ppm/˚C. Topographical surface images of as-grown and heat-treated films are shown in figure 5. The as-grown surface of x = 0 samples (figure 5a) appear

spherical in shape with average grain size 53 nm (±15). With inclusion of Cu dopant, x = 0.6 (figure 5b), the grains appear to elongate with grain size of 89 nm on average with a variation of ±25 nm. The increase in grain size justifies the presence of a sharper (200) peak for the as-grown x = 0.6 films compared to x=0 and x=1 films observed in the XRD spectra in figure 4(a, b). For x=1 (figure 5c), a higher number of triangular shaped grains develop with average for grain size reducing to 80nm (±33) when compared to x=0.6 films (figure 5b). Topographical images of film samples with x = 0, 0.6 and 1 following heat treatment at 325°C are shown in figures 5 (d) to (f), respectively. The topology of the x = 0 film following heat treatment (figure 5d) appears to be more porous with increased grain size when compared to the film in the as-grown state (figure 5a).

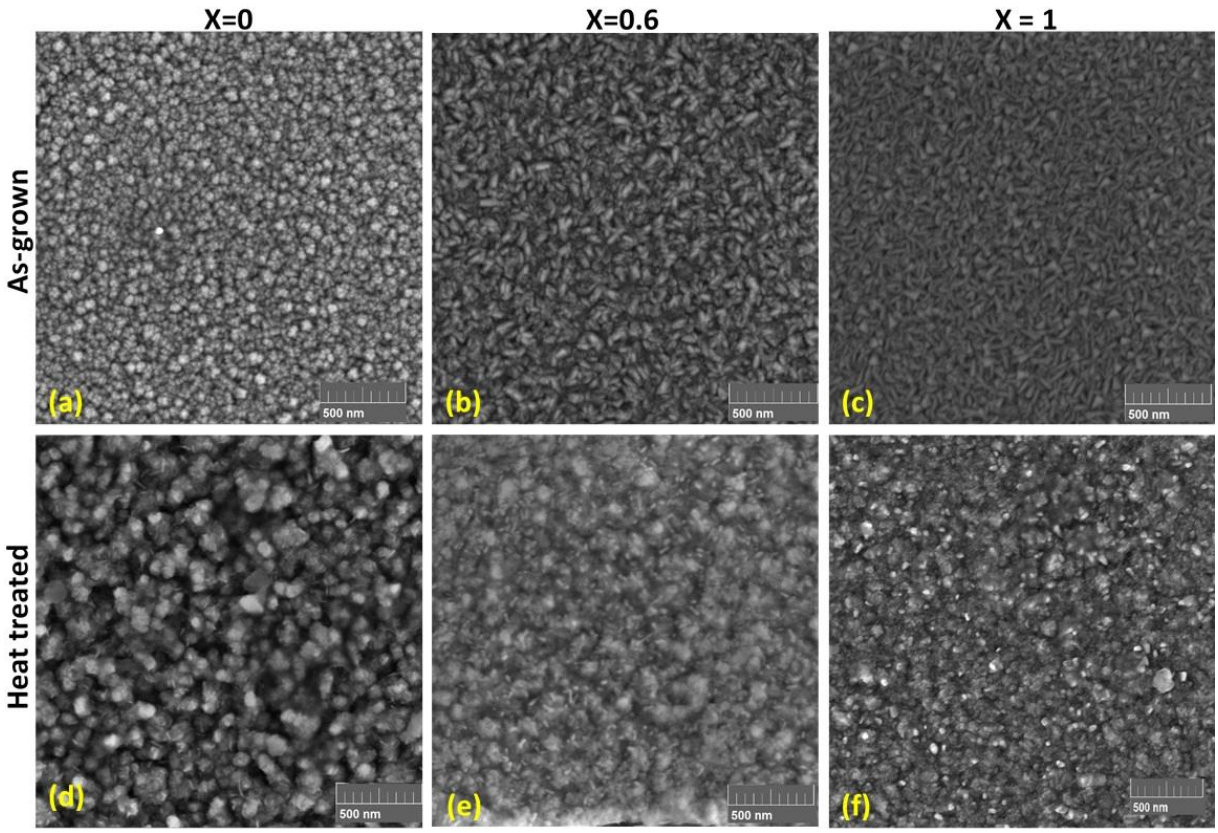

Figure 5: Surface topography of $Mn_3Ag_{(1-x)}Cu_{(x)}N$ films with x = 0, 0.6 and 1; as-grown (a-c) and after heat treatment at 325˚C (d-f).

Cross sectional images of as-grown and heat-treated films are shown in figure 6 (a) to (f). The thicknesses of the as-grown films (figure 6 (a)-(c)) measured on these SEM images are in the range 546 to 515 nm and have a columnar structure for all values of x. The uniformity of column width is very good for the x = 0 film (figure 6a) and becomes more random with increasing Cu concentrations at x = 0.6 (figure 6b) and x = 1 (figure 6c). Following heat treatment, the side profile of the x=0 film (figure 6d) is seen to become the most degraded. The porous nature of heat-treated topography of x=0 samples (figure 5d) seen earlier is again highlighted throughout the cross-sectional image (figure 6d). SEM images together with changes seen in XRD spectrum (figure 4 c) for Mn_3AgN films suggest that presence of Ag makes the antiperovskite structure unstable at higher heat treatment temperatures, which leads to loss of Mn from the antiperovskite structure, leading to formation of MnO on the upper layer of the film and a porous texture throughout the film and this is confirmed by SIMS data (figure 7) and cross section EDX (table 3) results in the following sections. Whereas for the films rich in Cu (x = 0.6 and 1), the underlying structure remains stable (figure 6e and f) and

following heat treatment the grains coalesce to form a more continuous upper layer on the film (figure 5e and f). This observation supports the claim that Cu in the upper layer is acting as a stabilizing element for the antiperovskite structure, prohibiting the loss of Mn from the structure at high temperature.

Table 2 shows a correlation between film composition and increase in film thickness and upper oxide layer, measured from the SEM cross section images. The thickness of the oxide layer for films with x = 0, 0.6 and 1 is measured to be 201, 107 and 89 nm, respectively, while the overall thickness of the thin film increases by 150, 55 and 17 nm from the original as-grown thickness, respectively. This indicates that in all three cases some part of the thin film antiperovskite structure disassociates at higher heat treatment temperature leading to formation of oxidised upper layers. The higher thickness of the upper layer for the x = 0 film compared to the x = 1 film correlates very well with the presence of pronounced Manganese oxide peaks in the XRD spectrums for Ag rich $Mn_3Ag_{(1-x)}Cu_{(x)}N$ films following heat treatment (figure 4b). These results promote that the larger shift towards a positive TCR with increasing heat treatment temperature observed in x = 0 films (figure 3(c)) is because of the increased oxygen content [53]. Therefore, with optimisation of Cu doping in the film, the formation of the upper oxide layer could be controlled and in turn, the TCR value could be fine-tuned towards zero.

Table 2: Thickness of $Mn_3Ag_{(1-x)}Cu_{(x)}N$ films with x=0, 0.6 and 1, as-grown and after heat treatment at 325˚C.

Value of x	As-grown thickness (nm)	After heat treatment at 325˚C	
		Upper layer thickness (nm)	Total thickness (nm)
0	546 ±7	201 ±18	694 ±15
0.6	503 ±8	107 ±4	558 ±4
1	516 ±14	89 ±3	533 ±4

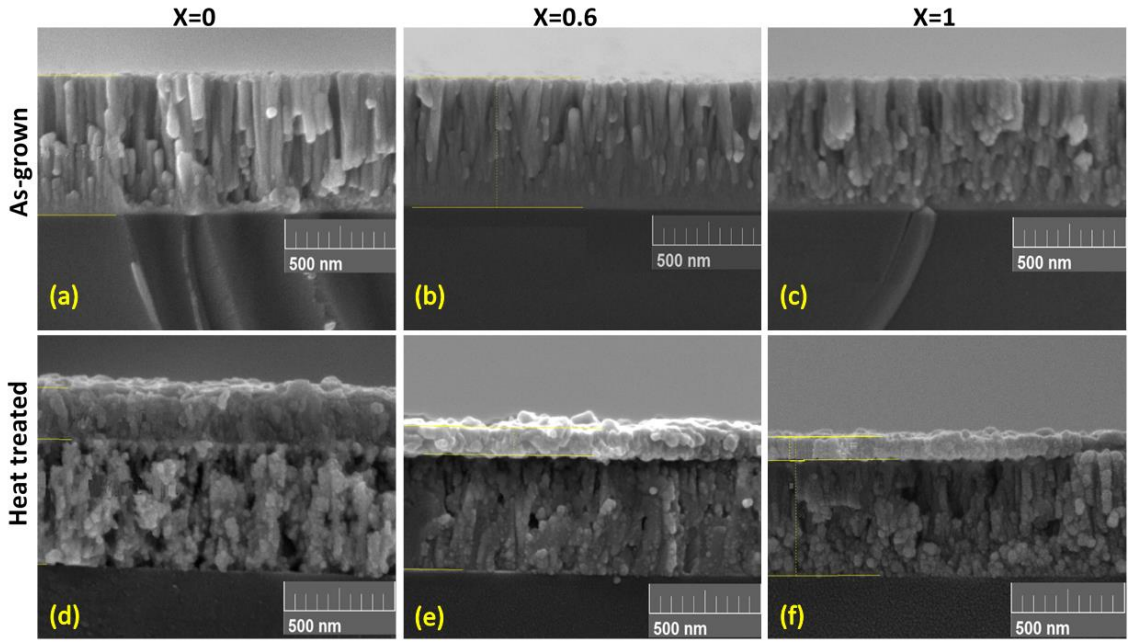

Figure 6: Cross sectional images of $Mn_3Ag_{(1-x)}Cu_{(x)}N$ films with x=0, 0.6 and 1; as-grown (a-c) and after heat treatment at 325˚C (d-f).

To better understand the chemical composition in the upper surface layers, depth profiles of the elements throughout the film thickness before and after heat treatment were acquired using SIMS. Figure 7 (a) and (b) shows the depth profile for Mn^{55+}, Cu^{63+}, and N^{14+} ions for x = 1 before and after heat treatment at 325˚C, respectively. In the as-grown state Mn^{55+}, Cu^{63+} and N^{14+} ions maintain a steady profile throughout the film thickness and the signal intensity for Mn^{55+} is greater than those for Cu^{63+} and N^{14+}. Following heat treatment (figure 7b), there is a migration of Mn^{55+} ions towards the film surface. The region where Mn^{55+} ions increase is accompanied by the withdrawal of Cu^{63+}, and N^{14+} ions to lower layers. This increase of Mn^{55+}, and reduction of Cu^{63+}, and N^{14+} ions is up to a depth of ~100 nm and is in agreement with the thickness of the upper oxide layer seen in figure 6(f). Therefore, by comparing SIMS and SEM data, it can be said that the upper surface layers formed during heat treatment are richer in Mn ions as Cu ions move to lower regions of the films.

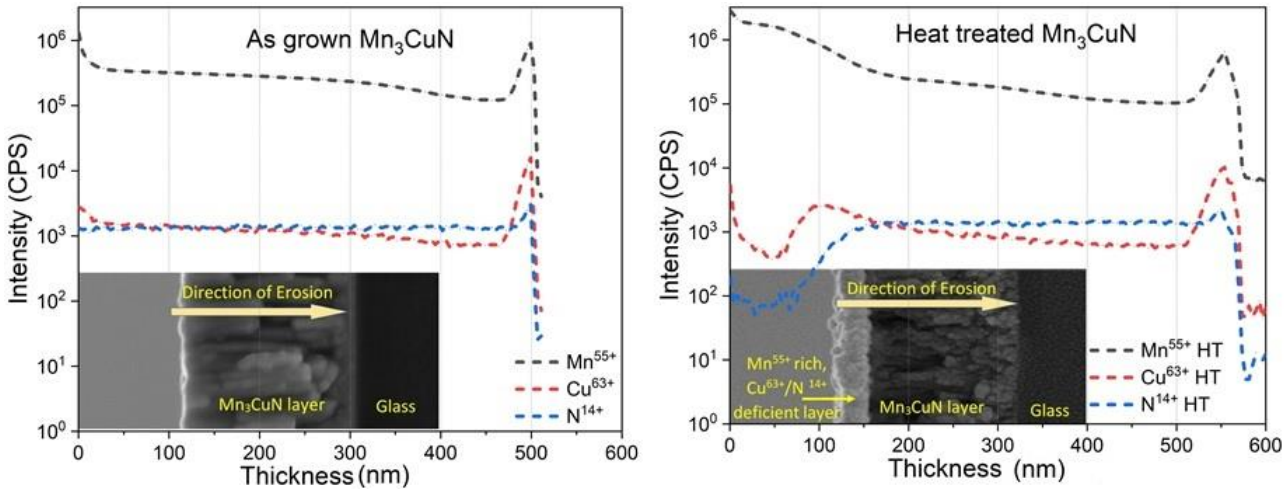

Figure 7: SIMS result for Mn_{55}^{+}, Cu_{63}^{+} and N_{14}^{+} in Mn_3CuN before and after heat treatment at 325°C. Thickness 0 nm indicates the start point on the surface of the film and the sharp drop in the element concentration represents the interface between the film and the glass substrate

In order to confirm the formation of manganese oxide and establish the true chemical composition of the upper film layer, low-voltage (5KeV) EDX was performed on the cross sections of $Mn_3Ag_{(1-x)}Cu_{(x)}N$ films with x=0, 0.6 and 1, heat-treated at 325˚C. The EDX results for the upper layer and lower layer are presented in Table 3 along with as the grown composition for comparison. It can be clearly seen that the upper layers of all three film compositions (x =0, 0.6 and 1) are very rich in oxygen, higher than 49 at.%. These layers also retain a high concentration (43.8 - 47.9 at %) of Manganese following heat treatment at 325˚C, while the concentration of secondary elements Ag or Cu drops to < 1.1 at.%. The upper layers are also deficient of Nitrogen with concentrations ranging between 2.3 – 6.4 at.%. This clearly shows the stronger oxidation of the upper layers of the Mn_3AgN antiperovskite structure during heat treatment and is in agreement with the SEM and XRD results so far. For the x=0 film, the underlying antiperovskite layer is also seen to be contaminated with a higher oxygen content of 17.3 at.% when compared to the Cu rich films (13.1/5.1 at.%). As discussed earlier, this result can be related to the porous structure of the Ag rich film exposing the underlying layer to more attack from oxygen. This increased porosity is attributed to higher surface activity in this film composition, which leads to removal of metal species from the cubic corners of the antiperovskite structure, making Mn available for oxidation to form MnO [52]. In the case x=1 films, the surface remains compact following heat treatment, thereby enabling the underlying layers to

maintain the antiperovskite structure as evidenced by the closer resemblance to the required 3:1:1 ratio and the lower oxygen concentration of 5.1 at.%.

Table 3 table of elemental composition of cross section of $Mn_3Ag_{(1-x)}Cu_{(x)}N$ films with x=0, 0.6 and 1 after heat treatment at 325°C.

x	Upper film layer	Lower film layer	As-grown
	Mn: Ag : Cu : N : O (at.%)	Mn: Ag :Cu : N : O(at.%)	Mn:Ag:Cu:N
0	46.0 : 1.1 : 0.0 : 3.8 : 49.1	41.9 : 19.0 : 0.0 : 22.5 : 17.3	57:20:0:23
0.6	43.8 : 0.0 : 0.6 : 6.4 : 49.2	56.9 : 4.1 : 9.9 : 16.7 : 13.1	60:9:11:20
1	47.9 : 0.0 : 0 6 : 2.3 : 49.2	55.4 : 0.0 : 20.9 : 18.6 : 5.1	57:0:23:20

Cross sectional images of x = 1 film samples as-grown and after heat treatment at 300, 325, 350 and 375˚C (Figure 8 (a)-(e)) clearly show that the thickness of the oxide layer is not only dependent on film composition but also on heat treatment temperature. This sample was selected for its combination of best dry heat stability test figure of 0.85% along with low TCR value of -25ppm/˚C among all the six film compositions. The variation of upper layer thickness with temperature, measured from the SEM images in figure 8, are reported in table 4 and can be corelated to the trend seen in sheet resistance earlier (reproduced in table 4) and the increase in sharpness of the oxide peaks observed in the XRD spectra of figure 4(b). The upper layer thickness increases slowly with increasing heat treatment temperature (56 and 89 nm for 300 and 325˚C respectively) and for these temperatures the combined effects of crystallization and defect healing overcomes this slow oxidation and results in an overall net reduction of sheet resistance. However, there is a drastic increment in the upper layer thickness of 157 and 175 nm when heat treated at 350 and 375˚C respectively, whereby the effect of oxidation becomes dominant and drives up the sheet resistance.

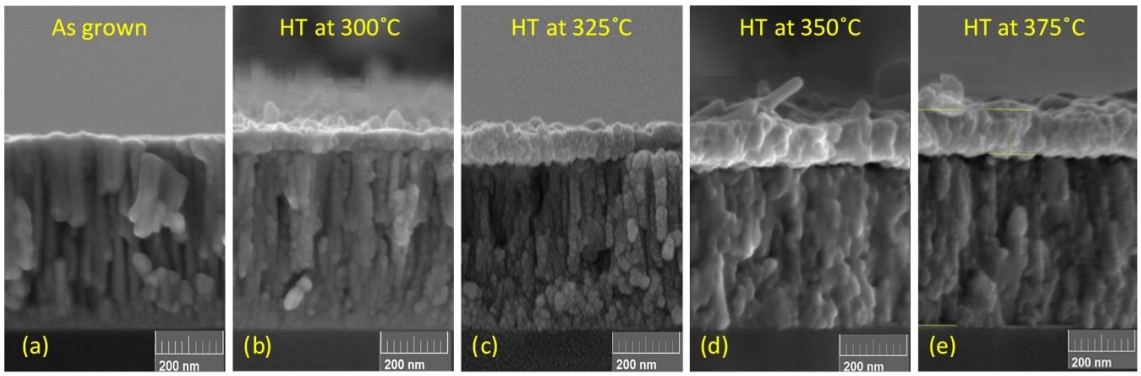

Figure 8: Cross sectional images of Mn_3CuN films after heat treatment at (a) 300˚C (b) 325˚C (c) 350˚C and (d) 375˚C .

Table 4: Thickness of Mn_3CuN films before and after heat treatment at 300˚C, 325˚C, 350˚C and 375˚C .

Heat treatment temperature (°C)	Upper layer thickness (nm)	Total thickness (nm)	Sheet resistance, Rs (Ω/□)
As-grown	0	516 ±14	21.95
300	56 ±8	529 ±5	19.21
325	89 ±3	533 ±4	18.90
350	157 ±9	617 ±7	22.24
375	175 ±22	603 ±12	27.96

To study the change in surface texture with increasing heat treatment temperature, AFM was employed to probe the surface of the x=1 films over an area of 3 μm^2, see figure 9 a-e. The as-grown film surface texture (figure 9a) is in agreement to the as-grown SEM image (figure 5c). The grains appear spherical with uniform height and dispersion across the surface. The vertical height of the grains is limited to <60 nm with an average RMS surface roughness value of 5.18 nm. With heat treatment temperature of 300 and 325˚C, the surface shows grain growth with columns growing in height due to the agglomeration of smaller grains and reaches vertical scales of <230 and <290 nm accompanied by an increase of surface roughness to 26.44 and 29.43nm respectively. However, after heat treatment at 350˚C, the grains suddenly change in nature and become finer and fibrous with a vertical scale reduced to <100 nm. This is also reflected in reduction in the measured surface roughness to 11.81 nm. This sudden change in surface texture of the film can be associated with the more rapid oxidation of the upper layer which reduces the surface roughness. With further heat treatment at 375˚C, these fibre-like grains appear to grow in size and the surface becomes more compact. The vertical scale limit increases to ~120 nm and the surface roughness to 16.38 nm and combining this with the cross section EDX results earlier, supports further oxidation of the upper layer at this temperature. These results strongly support that Mn_3CuN antiperovskite films undergo crystallization up to heat treatment temperatures of 325˚C, also seen earlier by the grain growth and XRD results in figure 4, whereas at temperatures of 350˚C and above, oxidation of the upper surface becomes the dominant mechanism, as shown in the continuous increase in the thickness of the upper layer. Therefore, by refining the heat treatment temperature and chemical composition, it is possible to control the crystallinity of the film, oxidation rate and surface texture of the upper layer, which in turn directly affect the dominant electrical conduction mechanisms. This process could be used as a calibration tool to fine tune the resistance stability and TCR of $Mn_3Ag_{(1-x)}Cu_{(x)}N$ films to near zero values.

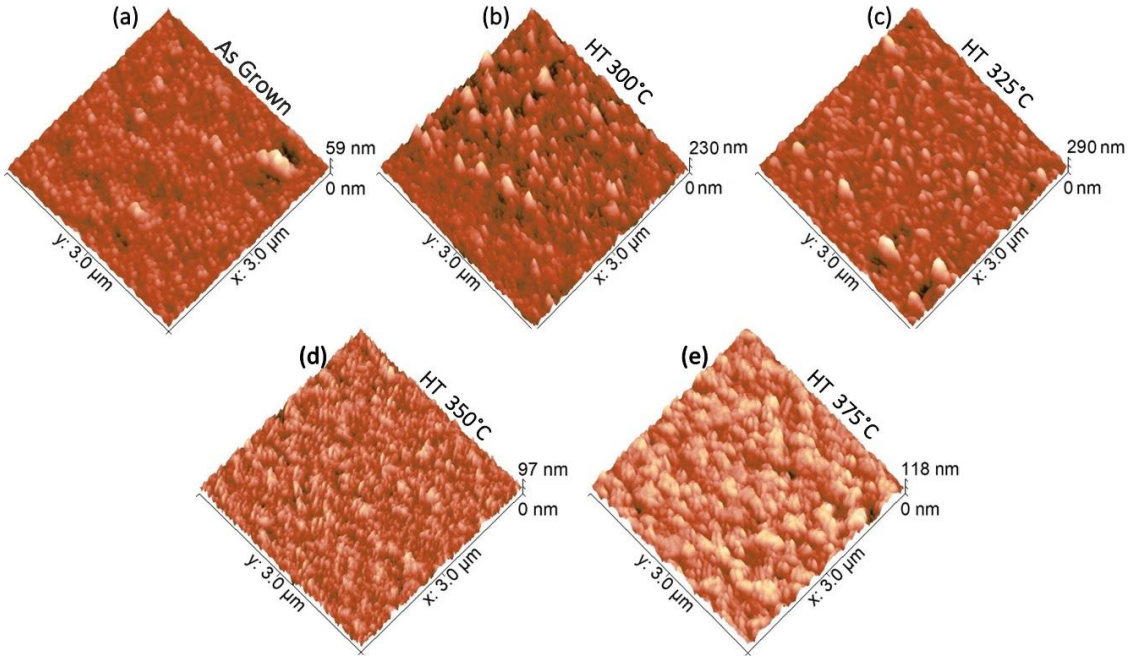

Figure 9: Atomic force microscopy images of Mn_3CuN film (a) as-grown and after heat treatment at (b)300˚C (C) 325˚C (d) 350˚C (e) 375˚C

4. Conclusion

This study has successfully demonstrated the sputter deposition of $Mn_3Ag_{(1-x)}Cu_{(x)}N$ antiperovskite thin films with extremely low TCR values. XRD analysis showed that the as-grown films were single phase, cubic structures with preferential alignment along the (200) plane for the ternary composition range of the experiment (x = 0.2, 0.4 and 0.6). Following heat treatment, all films showed improved crystallinity with additional peaks representing oxides of manganese. EDX and SIMS results confirmed the formation of manganese oxides at the surface, and these are more prominent for Ag rich films and dependent on the heat treatment temperature. All ternary structures showed as-grown negative values of TCR in the range of -233 to -351 ppm/˚C. However, with heat treatment in the temperature range of 325-350 ˚C, these values shifted to near zero values of ±30 ppm/˚C, with the most favourable value of TCR of -4.66 ppm/˚C observed for $Mn_3Ag_{0.4}Cu_{0.6}N$ films after heat treatment at 350 ˚C. The stabilization treated Mn_3CuN samples registered an excellent resistance stability figure of 0.85% following storage for one week at 155 ˚C. The balance between recrystallization, defect healing and surface oxidation, steers the sheet resistance value and TCR value of Mn_3AgN, controlled by the doping concentration of Cu in the film and post deposition heat treatment temperature. Therefore, with precise control of the Ag/Cu concentration and heat treatment conditions, $Mn_3Ag_{(1-x)}Cu_{(x)}N$ thin films can be fine-tuned for application requiring TCR values better than ±5 ppm/˚C and stability better than 1% operating in temperatures up to 155 ˚C.

Acknowledgements

This work was supported by a collaborative partnership between Northumbria University and TT Electronics PLC, Bedlington, UK. TT Electronics PLC, Bedlington, UK supplied the prescribed alumina substrates with silver conductor pads used in this experiment. IRC TT, Corpus Christi, USA, a

subsidiary of TT Electronics PLC, shared insight into key production stages of extremely low TCR passive components.

References

1. Morral, F.R., *The constitution of iron rich Fe-Al-C alloys.* Journal Iron and Steel institute London 1934. **130** p. 419-430.
2. Yin, Y., et al., *Critical behavior in the antiperovskite Mn3CuN at ferromagnetic to paramagnetic phase transition.* Journal of Magnetism and Magnetic Materials, 2013. **346**: p. 203-208.
3. Chu, L.-H., et al., *Doping Effect of Co at Ag Sites in Antiperovskite Mn3AgN Compounds.* Chinese Physics Letters, 2015. **32**(4): p. 047501.
4. Benmalem, Y., et al., *Thermoelectric, electronic and structural properties of CuNMn3 cubic antiperovskite.* Journal of Computational Electronics, 2018. **17**(3): p. 881-887.
5. Guo, X., et al., *Effects of Cr Substitution on Negative Thermal Expansion and Magnetic Properties of Antiperovskite Ga1-x Cr x N0.83Mn3 Compounds.* Front Chem, 2018. **6**: p. 75.
6. Zhou, C., et al., *Fully-dense Mn3Zn0.7Ge0.3N /Al composites with zero thermal expansion behavior around room temperature.* Materialia, 2019. **6**.
7. Cao, H., et al., *Microstructural characterization, mechanical properties and thermal expansion of antiperovskite manganese nitride Mn3.1Zn0.5Sn0.4N fabricated by combing vacuum sintering and spark-plasma sintering.* Materials Characterization, 2020. **160**.
8. Tong, P., et al., *Magnetic transition broadening and local lattice distortion in the negative thermal expansion antiperovskite Cu1−xSnxNMn3.* Applied Physics Letters, 2013. **102**(4): p. 041908.
9. Shibayama, T. and K. Takenaka, *Giant magnetostriction in antiperovskite Mn3CuN.* Journal of Applied Physics, 2011. **109**(7): p. 07A928.
10. Na, Y., et al., *Structure and properties of ternary manganese nitride Mn3CuNy thin films fabricated by facing target magnetron sputtering.* Materials Research Bulletin, 2011. **46**(7): p. 1022-1027.
11. Wang, Y., et al., *Antiperovskites with Exceptional Functionalities.* Adv Mater, 2020. **32**(7): p. e1905007.
12. Durai, G., et al., *Supercapacitive properties of manganese nitride thin film electrodes prepared by reactive magnetron sputtering: Effect of different electrolytes.* Ceramics International, 2019. **45**(14): p. 17120-17127.
13. Zhang, X.H., et al., *Observation of spin-glass behavior in antiperovskite compound Mn3Cu0.7Ga0.3N.* Applied Physics Letters, 2013. **103**(2): p. 022405.
14. Sun, Y., et al., *Low temperature coefficient of resistivity induced by magnetic transition and lattice contraction in Mn3NiN compound.* Scripta Materialia, 2010. **62**(9): p. 686-689.
15. Chu, L., et al., *Unusual Electrical Transport Driven by the Competition between Antiferromagnetism and Ferromagnetism in Antiperovskite Mn(3)Zn1-xCoxN.* Materials (Basel), 2018. **11**(2).
16. Wang, F., K. Li, and N.G. Zhou, *Structural, electronic properties and stability of AlCMn3 (111) surfaces by first-principles calculations.* Applied Surface Science, 2014. **289**: p. 351-357.
17. Lin, J.C., et al., *Tunable temperature coefficient of resistivity in C- and Co-doped CuNMn3.* Scripta Materialia, 2011. **65**(5): p. 452-455.
18. Dawson, J.A., et al., *Elucidating lithium-ion and proton dynamics in anti-perovskite solid electrolytes.* Energy & Environmental Science, 2018. **11**(10): p. 2993-3002.
19. Yin, L., et al., *Engineering Frenkel defects of anti-perovskite solid-state electrolytes and their applications in all-solid-state lithium-ion batteries.* Chemical Communications, 2020. **56**(8): p. 1251-1254.
20. Zhao, W., et al., *Solid-State Electrolytes for Lithium-Ion Batteries: Fundamentals, Challenges and Perspectives.* Electrochemical Energy Reviews, 2019. **2**(4): p. 574-605.
21. Wu, M., et al., *First-principles study on the structural, electronic, and Li-ion mobility properties of anti-perovskite superionic conductor Li3OCl (1 0 0) surface.* Applied Surface Science, 2020. **510**.
22. E.O.Chi, W.S.Kim, and N.H.Hur, *nearly zero temperature coefficient of resistiivty in antiperovskite compound CuNMn3.* Solid state communication 2001. **120**: p. 307-310.
23. Fruchart, D. and E. F. Bertaut, *Magnetic Studies of the Metallic Perovskite-Type Compounds of Manganese.* Journal of the Physical Society of Japan, 1978. **44**(3): p. 781-791.

24. Lu, N.P., et al., *Ternary Mn3NMn1−xAgxcompound films of nearly constant electrical resistivity and their magnetic transport behaviour.* Journal of Physics D: Applied Physics, 2016. **49**(4): p. 045308.
25. K. Momma and F. Izumi, V.f.t.-d.v.o.c., volumetric and morphology data," J. Appl. Crystallogr., 44, 1272-1276 (2011).
26. Ying, S., et al., *Investigation of antiperovskite Mn3CuNx film prepared by DC reactive magnetron sputtering.* Materials Research Bulletin, 2010. **45**(9): p. 1230-1233.
27. Lei, D., et al., *Near zero temperature coefficient of resistivity in antiperovskite Mn3Ni1−xCuxN.* Applied Physics Letters, 2011. **99**(25): p. 251905.
28. Hui, Z., et al., *Synthesis and Physical Properties of Antiperovskite CuNFe3 Thin Films via Solution Processing for Room Temperature Soft-Magnets.* Coatings, 2020. **10**(3).
29. Bilal, M., et al., *Electronic Properties of Antiperovskite Materials from State-of-the-Art Density Functional Theory.* Journal of Chemistry, 2015. **2015**: p. 1-11.
30. Ying, S., et al., *The Unusual Resistivity Behavior and Correlated Magnetic Properties of Antiperovskite Mn3Ag[1−x]M[x]N (M = Sn, Zn) Compounds.* Science of Advanced Materials, 2014. **6**(7): p. 1394-1398.
31. Takenaka, K., et al., *Extremely low temperature coefficient of resistance in antiperovskite Mn[sub 3]Ag[sub 1−x]Cu[sub x]N.* Applied Physics Letters, 2011. **98**(2): p. 022103.
32. Oe, T., et al., *Optimization ofMn3Ag1−xCuxN Antiperovskite Compound Fabrication for Resistance Standard.* IEEE TRANSACTIONS ON INSTRUMENTATION AND MEASUREMENT, 2013. **62** (6): p. 4.
33. Baunack, S., et al., *Auger electron spectroscopy study of interdiffusion, oxidation and segregation during thermal treatment of NiCr/CuNi(Mn)/NiCr thin films.* Applied Surface Science, 1999. **144-145**: p. 216-221.
34. Masahiro, A., T. Koshi, and I. Hiroshi, *Sputter deposition and characterization of Mn3CuN thin films.* Journal of Alloys and Compounds, 2013. **577**: p. S314-S317.
35. Wang, X.Y., et al., *Deposition of Cr–Si–Ni–Mo films at a low sputtering current and performance of heat and humid resistance.* Applied Surface Science, 2014. **289**: p. 538-544.
36. Rahm, M., R. Hoffmann, and N.W. Ashcroft, *Atomic and Ionic Radii of Elements 1–96.* Chem. Eur. J, 2016: p. 14625 – 14632.
37. Matula, R.A., *Electrical resistivity of copper, gold, palladium, and silver.* Journal of Physical and Chemical Reference Data, 1979. **8**(4): p. 1147-1298.
38. THANIGAIMANI, V. and M.A. ANGADI, *Thickness dependence of temperature coefficient of resistance and neel temperature in MnTe films* JOURNAL OF MATERIALS SCIENCE LETTERS 1993. **12**: p. 1052-1056.
39. Hahtela, O., et al., *Atomic layer deposited alumina (Al<inf>2</inf>O<inf>3</inf>) coating on thin film cryoresistors*, in *2008 Conference on Precision Electromagnetic Measurements Digest*. 2008. p. 272-273.
40. A. Boogaard, J.J.v.d.B., *Crystallisation and electrical resistivity of sputter-deposited aluminium–germanium alloy films.* Thin Solid Films, 2001. **401**: p. 1–6.
41. De Los Santos Valladares, L., et al., *Crystallization and electrical resistivity of Cu2O and CuO obtained by thermal oxidation of Cu thin films on SiO2/Si substrates.* Thin Solid Films, 2012. **520**(20): p. 6368-6374.
42. Ramana, C.V., et al., *Chemical bonding, optical constants, and electrical resistivity of sputter-deposited gallium oxide thin films.* Journal of Applied Physics, 2014. **115**(4).
43. Jui Chang Chuang, M.-C.C., *Properties of thin Ta-N films reactively sputtered on Cu/SiO_2/Si substrates.* Thin Solid Films, 1998. **322**: p. 213-217.
44. Karmakar, R., et al., *Structural, Morphological, Optical and Magnetic Property of Mn doped Ferromagnetic ZnO thin film* Applied Surface Science, 2012. **263**(15): p. 671-677.
45. Barpanda, P., et al., *Structure and electrochemical properties of novel mixed Li(Fe1-xMx)SO4F (M = Co, Ni, Mn) phases fabricated by low temperature ionothermal synthesis.* Journal of Materials Chemistry 2010.
46. Muniz, F.T., et al., *The Scherrer equation and the dynamical theory of X-ray diffraction.* Acta Crystallogr A Found Adv, 2016. **72**(Pt 3): p. 385-90.
47. Kim, J., et al., *Electrical Properties of Zn(Mn,Co)O Films Grown by Pulsed Laser Deposition Method.* ECS Transactions, 2008. **16**(12): p. 27-31.

48. Mosquera, A.A., et al., *Effect of silver on the phase transition and wettability of titanium oxide films.* Sci Rep, 2016. **6**: p. 32171.
49. Ju, H., et al., *Microstructure, mechanical and tribological properties of TiN-Ag films deposited by reactive magnetron sputtering.* Vacuum, 2017. **141**: p. 82-88.
50. Lopes, C., et al., *Evolution of the functional properties of titanium–silver thin films for biomedical applications: Influence of in-vacuum annealing.* Surface and Coatings Technology, 2015. **261**: p. 262-271.
51. Lopes, C., et al., *Study of the electrical behavior of nanostructured Ti–Ag thin films, prepared by Glancing Angle Deposition.* Materials Letters, 2015. **157**: p. 188-192.
52. Zhao, H., et al., *Surface activity of antiperovskite manganese nitrides.* Journal of Materials Research, 2013: p. 1-7.
53. Jia, Q.X., et al., *Stable thin film resistors using double layer structure.* Journal of Materials Research, 2011. **10**(6): p. 1523-1528.

Supplementry Information :

1. Plot of thickness increment vs Sheet resistance for Mn_3CuN films.